

DYNAMICAL MASS OF THE M8+M8 BINARY 2MASS J22062280–2047058AB^{*,†,‡,**}

TRENT J. DUPUY, MICHAEL C. LIU,¹ AND BRENDAN P. BOWLER
Institute for Astronomy, University of Hawai‘i, 2680 Woodlawn Drive, Honolulu, HI 96822
Submitted to ApJ 2009 May 26; accepted 2009 September 24

ABSTRACT

We present Keck laser guide star adaptive optics imaging of the M8+M8 binary 2MASS J2206–2047AB. Together with archival *HST*, Gemini-North, and VLT data, our observations span 8.3 years of the binary’s 35_{-5}^{+6} year orbital period, and we determine a total dynamical mass of $0.15_{-0.03}^{+0.05} M_{\odot}$, with the uncertainty dominated by the parallax error. Using the measured total mass and individual luminosities, the Tucson and Lyon evolutionary models both give an age for the system of $0.4_{-0.2}^{+9.6}$ Gyr, which is consistent with its thin disk space motion derived from the Besançon Galactic structure model. Our mass measurement combined with the Tucson (Lyon) evolutionary models also yields precise effective temperatures, giving 2660_{-100}^{+90} K and 2640_{-100}^{+90} K (2550_{-100}^{+90} K and 2530_{-100}^{+90} K) for components A and B, respectively. These temperatures are in good agreement with estimates for other M8 dwarfs (from the infrared flux method and the M8 mass benchmark LHS 2397aA), but atmospheric model fitting of the integrated-light spectrum gives hotter temperatures of 2800 ± 100 K for both components. This modest discrepancy can be explained by systematic errors in the atmospheric models or by a slight underestimate of the distance (and thus mass and age) of the system. We also find the observed near-infrared colors and magnitudes do not agree with those predicted by the Lyon Dusty models, given the known mass of the system.

Subject headings: binaries: close — binaries: general — binaries: visual — infrared: stars — stars: low-mass, brown dwarfs — techniques: high angular resolution

1. INTRODUCTION

Direct mass measurements are a key underpinning of stellar astronomy, as the characteristics of stars depend more strongly on mass than any other property. However, there are only a handful of mass measurements available for the lowest mass stars ($M < 0.1 M_{\odot}$), which largely comes from work conducted more than a decade ago (e.g., Henry & McCarthy 1993; Ségransan et al. 2000). This is because such measurements were limited by the scarce number of low-mass objects known, until wide-field optical and infrared surveys enabled the discovery of hundreds more (e.g., Gizis et al. 2000) and high-resolution imaging campaigns identified dozens of visual binaries among these objects (e.g., Close et al.

2002; Bouy et al. 2003). Today, many of these binaries are finally yielding dynamical mass measurements after years of patient orbital monitoring (e.g., Seifahrt et al. 2008; Dupuy et al. 2009b).

The M8 dwarf 2MASS J22062280–2047058 (hereinafter 2MASS J2206–2047) was discovered in the Two Micron All Sky Survey (2MASS) by Gizis et al. (2000) and was revealed to be a binary by Close et al. (2002). Costa et al. (2006) measured a trigonometric parallax for the system of 37.5 ± 3.4 mas, corresponding to a distance of $26.7_{-2.1}^{+2.6}$ pc. We present here a dynamical mass for 2MASS J2206–2047AB based on Keck laser guide star adaptive optics (LGS AO) imaging from our ongoing orbital monitoring program targeting ultracool binaries. Combining our Keck data with archival *Hubble Space Telescope* (*HST*), Very Large Telescope (VLT), and Gemini-North Telescope images, we measure a total mass of $0.15_{-0.03}^{+0.05} M_{\odot}$, with the dominant source of uncertainty being the 9.1% error in the parallax, which translates into an asymmetric $_{-22}^{+32}$ % error in the mass. Despite the relatively large uncertainty in the mass, our measurement reveals significant discrepancies between the predictions of evolutionary and atmospheric models and the observed properties of 2MASS J2206–2047AB.

2. OBSERVATIONS

2.1. *Keck/NIRC2 LGS*

We monitored 2MASS J2206–2047AB using the LGS AO system at the Keck II Telescope on Mauna Kea, Hawaii (Wizinowich et al. 2006; van Dam et al. 2006), using the facility near-infrared camera NIRC2 in its narrow field-of-view mode. At each epoch, we obtained data in one or more filters covering the standard atmospheric windows from the Mauna Kea Observatories (MKO) fil-

* Some of the data presented herein were obtained at the W.M. Keck Observatory, which is operated as a scientific partnership among the California Institute of Technology, the University of California, and the National Aeronautics and Space Administration. The Observatory was made possible by the generous financial support of the W.M. Keck Foundation.

† Based partly on observations made with the NASA/ESA *Hubble Space Telescope*, obtained from the data archive at the Space Telescope Institute. STScI is operated by the association of Universities for Research in Astronomy, Inc. under the NASA contract NAS 5-26555.

‡ Based partly on observations obtained under program ID GN-2001B-C-2 at the Gemini Observatory, which is operated by the Association of Universities for Research in Astronomy, Inc., under a cooperative agreement with the NSF on behalf of the Gemini partnership: the National Science Foundation (United States), the Science and Technology Facilities Council (United Kingdom), the National Research Council (Canada), CONICYT (Chile), the Australian Research Council (Australia), Ministério da Ciência e Tecnologia (Brazil) and SECYT (Argentina).

§ Based partly on observations made with ESO Telescopes at the Paranal Observatory under program IDs 071.C-00327 and 077.C-0062.

¹ Alfred P. Sloan Research Fellow

TABLE 1
KECK LGS AO OBSERVATIONS

Date (UT)	Time (UT)	Airmass	Filter	FWHM (mas)	Strehl ratio
2008 May 29	14:55	1.375	K_S	54.7 ± 0.7	0.387 ± 0.017
2008 Sep 8	08:32	1.345	J	52 ± 3	0.050 ± 0.008
	08:27	1.352	H	51 ± 3	0.145 ± 0.015
	08:21	1.362	K_S	53.6 ± 1.1	0.368 ± 0.019
	08:47	1.328	L'	84 ± 2	0.67 ± 0.18
2008 Dec 1	05:29	1.482	K_S	101 ± 6	0.047 ± 0.010

ter consortium (Simons & Tokunaga 2002; Tokunaga et al. 2002). The LGS provided the wavefront reference source for AO correction, with the exception of tip-tilt motion. The LGS brightness, as measured by the flux incident on the AO wavefront sensor, was equivalent to a $V \approx 10.1\text{--}10.7$ mag star. The tip-tilt correction and quasi-static changes in the image of the LGS as seen by the wavefront sensor were measured contemporaneously by a second, lower bandwidth wavefront sensor monitoring 2MASS J2206–2047, which saw the equivalent of an $R \approx 15.8\text{--}16.2$ mag star.

Our procedure for obtaining, reducing, and analyzing our images is described in detail by Dupuy et al. (2009b). Table 1 summarizes our observations of 2MASS J2206–2047AB, and typical images from each data set are shown in Figure 1. The binary separation, position angle (P.A.), and flux ratio were determined using the same three-component Gaussian representation of the point-spread function (PSF) as described in Dupuy et al. (2009b). We used the astrometric calibration from Ghez et al. (2008), with a pixel scale of 9.963 ± 0.005 mas pixel $^{-1}$ and an orientation for the detector’s $+y$ -axis of $+0^\circ.13 \pm 0^\circ.02$ east of north, and applied the distortion correction developed by B. Cameron (2007, private communication), which changed the results below the 1σ level.

To assess systematic errors in our PSF-fitting procedure, we also applied it to simulated Keck images of 2MASS J2206–2047AB that were created using images of PSF reference sources with similar FWHM and Strehl, summarized in Table 2. After being reduced in an identical fashion to the science images, the individual dithered images were shifted with interpolation and added to themselves to match the observed binary configuration at each epoch. These simulated images were then fit in an identical manner to the science images, and the rms and mean of the truth-minus-fitted parameters determined the uncertainty and systematic offset.

For the 2008 May and December K_S band data, the simulations predicted insignificant systematic offsets ($\lesssim 0.3\sigma$) and rms errors that were somewhat smaller than the rms of individual science dithers. For these data sets, we adopted the science rms values for the errors in all binary parameters and did not apply the Monte Carlo offsets. For the 2008 September data (J , H , K_S , and L' bands), our simulations yielded significant systematic offsets (as large as 2.4σ in L' band) and errors that were consistent with or somewhat smaller than the rms of individual science dithers. Such offsets are expected, particularly in high-Strehl images with prominent Airy rings, as our multi-Gaussian PSF model is known to be an imper-

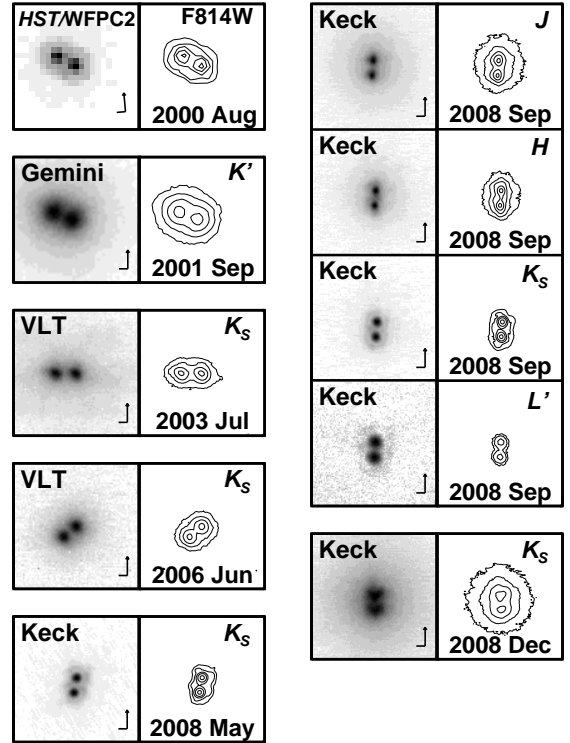


FIG. 1.— *HST*, Gemini, VLT, and Keck images of 2MASS J2206–2047AB shown chronologically by column. All images are shown on the same scale, $1''$ on a side, using a square-root stretch for the grayscale images. We do not rotate the *HST* data so that north is up in order to preserve the somewhat undersampled nature of the WFC2 data. The Airy ring of the Keck PSF is visible in some Keck images. Contours are drawn at 0.78, 0.37, 0.18, 0.085, and 0.040 of the peak pixel. The lowest contour is not drawn for the Gemini, VLT, and 2008 December Keck images. The lowest two contours are not drawn for the Keck L' band images.

fect representation of the data. Because we had data in four bandpasses at a single epoch, we were able to check that the Monte Carlo offsets brought the astrometry into better agreement – if they did not, our simulations would not have correctly assessed our systematic errors. We used the Monte Carlo-derived errors to compute χ^2 for the separation and P.A. measurements and found that after applying the systematic offsets χ^2 improved from 17.3 to 2.4 for the separation and from 7.8 to 1.3 for the P.A. (n.b., since there are 3 degrees of freedom, the median value of χ^2 is 2.4). Thus, we applied the systematic offsets from our Monte Carlo simulations as they brought the multiband astrometry into agreement, and we adopted the Monte Carlo errors if they were larger than the rms of measurements from individual images.

A summary of the astrometry and flux ratios derived from the Keck data is given in Table 3. We used the data set with the smallest astrometric errors at each epoch in the orbit fit. As discussed in Section 3.1, the resulting orbit fit changes insignificantly if we vary the input astrometry by: (1) using the errors and offsets derived from Monte Carlo simulations rather than simply using the rms of individual dithers for the errors; (2) using a

TABLE 2
KECK PSF REFERENCE OBSERVATIONS

Date (UT)	Time (UT)	Airmass	Filter	FWHM (mas)	Strehl ratio
2008 May 29 ^a	13:17	1.162	K_S	55.5 ± 0.8	0.395 ± 0.020
2008 Sep 8 ^b	09:15	1.333	J	52 ± 3	0.054 ± 0.003
	09:06	1.343	H	51 ± 2	0.145 ± 0.016
	09:00	1.350	K_S	53.0 ± 0.9	0.348 ± 0.007
	09:21	1.328	L'	84 ± 2	0.42 ± 0.16
	06:16	1.329	K_S	97 ± 12	0.049 ± 0.014
2008 Dec 1 ^c					

^a2MASS J17502484–0016151

^b2MASS J22345725–2101071

^c2MASS J21402966+1625212

different data set for a given epoch.

2.2. *HST*/WFPC2-PC1

Bouy et al. (2003) reported binary parameters for 2MASS J2206–2047AB based on their *HST* discovery images; however, we have chosen to re-analyze this data because in our previous work we have found that our PSF fitting technique can yield somewhat more precise astrometry (Liu et al. 2008). Also, Bouy et al. (2003) did not derive individual measurement errors for each binary in their sample, and accurate uncertainties are critical for orbit fitting. We retrieved the *HST* archival images of 2MASS J2206–2047AB obtained with the WFPC2 Planetary Camera (PC1) on UT 2000 August 13 (GO-8581, PI Reid). These comprise two 30 s exposures in the F814W bandpass and one 500 s F1042M exposure. We only used the F814W images for deriving astrometry because (1) the smaller PSF enables better deblending of this tight binary and (2) a pair of images offers better cosmic ray rejection than a single image. We used TinyTim (Krist 1995) to generate PSF models which were fit to the data in a similar fashion to our previous work (Liu et al. 2008; Dupuy et al. 2009a). From our PSF fitting of the two images we determined the binary separation, position angle, and flux ratio.²

To determine uncertainties and potential systematic offsets for our measurements, we simulated images of 2MASS J2206–2047AB using images of single ultracool objects from other *HST*/WFPC2 programs (GO-8563, PI Kirkpatrick; GO-8581, PI Reid; and GO-8146, PI Reid). We only used objects with an equivalent or higher signal-to-noise ratio (S/N) compared to the science data so that we could degrade the S/N of the single images to match the science data. We also restricted ourselves to observations consisting of two or more images to allow robust rejection of cosmic rays. We only shifted images by an integer number of pixels to preserve the somewhat undersampled nature of the WFPC2 data. However, we were able to reproduce the binary configuration of 2MASS J2206–2047AB to within 0.2 pixels of the actual (Δx , Δy) separation of (+3.2, –1.6) pixels by carefully selecting appropriate pairs of input PSFs whose sub-pixel positions were determined in advance by single TinyTim PSF fitting.

² We used a pixel scale of 45.54 ± 0.01 mas pixel^{–1}, the quoted pixel scale from the WFPC2 Instrument Handbook for Cycle 13, which is consistent with other values in the literature (e.g., see the discussion by Liu et al. 2008).

We fitted the simulated binary images with TinyTim PSFs in the same way as the science data. The resulting rms scatter of the truth-minus-fitted parameters gave their errors, and the mean gave their systematic offsets. For both the separation and P.A., the offsets were small compared to the errors (-0.5 ± 1.8 mas and $-0^\circ.1 \pm 1^\circ.1$), but we found an offset in the flux ratio that was large compared to its rms error (-0.10 ± 0.02 mag). Since these errors in deblending the binary are due to small imperfections in the PSF model, it is natural that they would have the largest impact on the flux ratio, not positional measurements, since the cores of the PSFs are well-separated for this binary. In fact, because this binary has a flux ratio near unity, the systematic offset we found “flips” the binary, changing the component that is identified as the primary, and this flip brings the astrometry into agreement with the astrometry from other epochs.

We applied the systematic offsets from our simulations to the binary parameters, resulting in a separation of 161.1 ± 1.8 mas, a P.A. of $57^\circ.5 \pm 1^\circ.1$, and a flux ratio of 0.06 ± 0.02 mag (Table 3). We can compare these parameters to those derived by Bouy et al. (2003), who found a separation (163.0 ± 2.8 mas) and P.A. ($57^\circ.5 \pm 0^\circ.3$) consistent with our measurements. Our separation uncertainty is slightly smaller, and our P.A. uncertainty is larger. From their Figure 2, it is clear that our separation and P.A. errors are actually consistent with their analysis, and the apparent discrepancy between our errors only arises because they condense their detailed study of binary parameter uncertainties to a single number for the separation error and two numbers for the P.A. error ($0^\circ.3$ above separations of 150 mas; $1^\circ.2$ below 150 mas). For example, our P.A. error of $1^\circ.1$ is intermediate between their two values, which is reasonable for a binary with a separation very close to their cutoff between the two regimes. However, the flux ratio of 0.36 ± 0.07 mag derived by Bouy et al. (2003) is inconsistent with ours at 4σ . Because the measurement of the flux ratio is most sensitive to imperfections in the PSF model, it is natural that our different PSF fitting methods would disagree most on this parameter. We note that they apply a large 0.17 mag systematic offset to their flux ratio, which again is a single number condensed from more detailed analysis (see their Figure 3). This offset could account for 2.3σ of the discrepancy, which would bring our two flux ratios into reasonable agreement. The F814W flux ratio does not enter substantially into the following analysis, and so the discrepancy between our value and that of Bouy et al. (2003) has no impact on our results.

2.3. *Gemini*/Hokupa‘a

2MASS J2206–2047AB was imaged on UT 2001 September 22 by the Hokupa‘a curvature AO system at the Gemini-North Telescope on Mauna Kea, Hawai‘i. Analysis of these data has previously been presented by Close et al. (2002); however, we have conducted our own analysis in an attempt to reduce the astrometric errors. We retrieved these raw data from the Gemini science archive and registered, sky-subtracted, and performed cosmic ray rejection on the images. Figure 1 shows a typical image from one of the 15 K' band 10 s exposures which were used to derive the astrometry for 2MASS J2206–2047AB.

We used the same analytic PSF-fitting routine as

TABLE 3
BEST-FIT BINARY PARAMETERS FOR 2MASS J2206–2047AB

Epoch (UT)	Instrument	Filter	ρ (mas)	P.A. ($^\circ$)	Δm (mag)
2000 Aug 13	<i>HST</i> /WFPC2-PC1 ^a	F814W	161.1 \pm 1.8	57.5 \pm 1.1	0.06 \pm 0.02
2001 Sep 22	Gemini/Hokupa‘a ^a	<i>K'</i>	167.7 \pm 1.0	68.2 \pm 0.5	0.04 \pm 0.02
2003 Jul 11	VLT/NACO ^a	<i>H</i>	164.2 \pm 0.3	89.2 \pm 0.2	0.05 \pm 0.05
2006 Jun 28	VLT/NACO ^a	<i>K_S</i>	131.3 \pm 0.3	130.38 \pm 0.16	0.077 \pm 0.017
2008 May 29	Keck/NIRC2 ^a	<i>K_S</i>	119.32 \pm 0.14	170.07 \pm 0.11	0.067 \pm 0.010
2008 Sep 8	Keck/NIRC2	<i>J</i>	120.5 \pm 0.3	175.94 \pm 0.11	0.06 \pm 0.02
	Keck/NIRC2 ^a	<i>H</i>	120.2 \pm 0.3	176.05 \pm 0.10	0.065 \pm 0.017
	Keck/NIRC2	<i>K_S</i>	120.4 \pm 0.4	175.89 \pm 0.11	0.06 \pm 0.02
	Keck/NIRC2	<i>L'</i>	121.1 \pm 0.5	176.1 \pm 0.4	0.004 \pm 0.016
2008 Dec 1	Keck/NIRC2 ^a	<i>K_S</i>	121.4 \pm 1.0	180.9 \pm 0.8	0.06 \pm 0.06

^aUsed in the orbit fit.

for the Keck data to fit the Gemini images of 2MASS J2206–2047AB. Adopting an instrument pixel scale of 19.98 ± 0.08 mas pixel⁻¹ (F. Rigaut 2001, private communication), we found a separation of 167.7 ± 1.0 mas, where the uncertainty is the standard deviation of measurements from individual dithered images. This is in good agreement with the 168 ± 7 mas separation reported by Close et al. (2002). The improvement in the separation error may be attributed to the fact that Close et al. (2002) used the scatter among *J*, *H*, and *K'*-band images, whereas we have restricted our measurement to the bandpass with highest quality images (*K'* band). We found a *K'* band flux ratio of 0.04 ± 0.02 mag, which is consistent (at 1.1σ) with the flux ratio of 0.08 ± 0.03 mag derived by Close et al. (2002).

Unfortunately, we are not able to derive the correct value for the binary P.A. from the archive images. As reported by Close et al. (2002), the image rotator was turned off for these observations so that the pupil is aligned with the detector. Thus, there is an arbitrary rotation in the images, which is not recorded in the FITS headers, and this rotation changes during each data set. We were able to remove this changing rotation by subtracting the parallactic angle from the binary P.A. measured in the individual dithers, and the rms scatter among the resulting P.A. measurements was $0^\circ.4$. Adding in quadrature the $0^\circ.3$ error in the absolute orientation of Hokupa‘a/QUIRC that was adopted by Close et al. (2002) results in a P.A. error of $0^\circ.5$, which is identical to their P.A. uncertainty.

Given the good agreement between our derived parameters and those derived by Close et al. (2002), we adopt our own separation measurement because of the smaller uncertainty but the Close et al. (2002) P.A. measurement because of our inability to reconstruct the orientation of the archival images. As discussed in Section 3.1, this choice is validated by the resulting orbit fit having a reduced χ^2 near unity.

2.4. VLT/NACO

We retrieved archival images of 2MASS J2206–2047AB obtained with the VLT at Paranal Observatory on UT 2003 July 11 and 2006 June 28. These data were taken with the NACO adaptive optics system (Lenzen et al. 2003; Rousset

et al. 2003) using the N90C10 dichroic and S13 camera (13.221 ± 0.017 mas pixel⁻¹)³ at both epochs. We registered, sky-subtracted, and performed cosmic ray rejection on the raw archival images. The 2003 data comprise four *H* band 60 s exposures, and the 2006 data comprise 14 *K_S* band 60 s exposures. Typical images from each data set are shown in Figure 1.

We used the same analytic PSF-fitting routine as was used for the Keck data to fit the VLT images, and the results are summarized in Table 3. The uncertainties were determined from the standard deviation of measurements from individual dithers. Since no PSF star was observed contemporaneously with 2MASS J2206–2047AB,

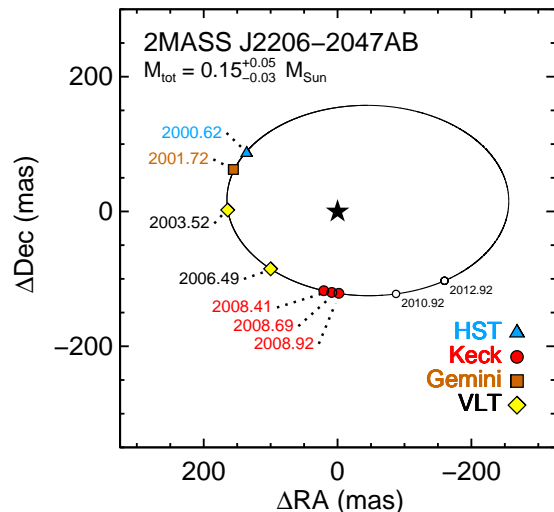


FIG. 2.— Relative astrometry along with the best fitting orbit for 2MASS J2206–2047AB (reduced χ^2 of 1.07 for 7 degrees of freedom). The empty circles show the predicted location of 2MASS J2206–2047B in the future. Error bars are smaller than the plotting symbols. The orbit is sufficiently well constrained that the uncertainty in the total mass is dominated by the 9.1% parallax error.

³ http://www.eso.org/sci/facilities/paranal/instruments/naco/doc/VLT-MAN-ESO-14200-2761_v83.3.pdf

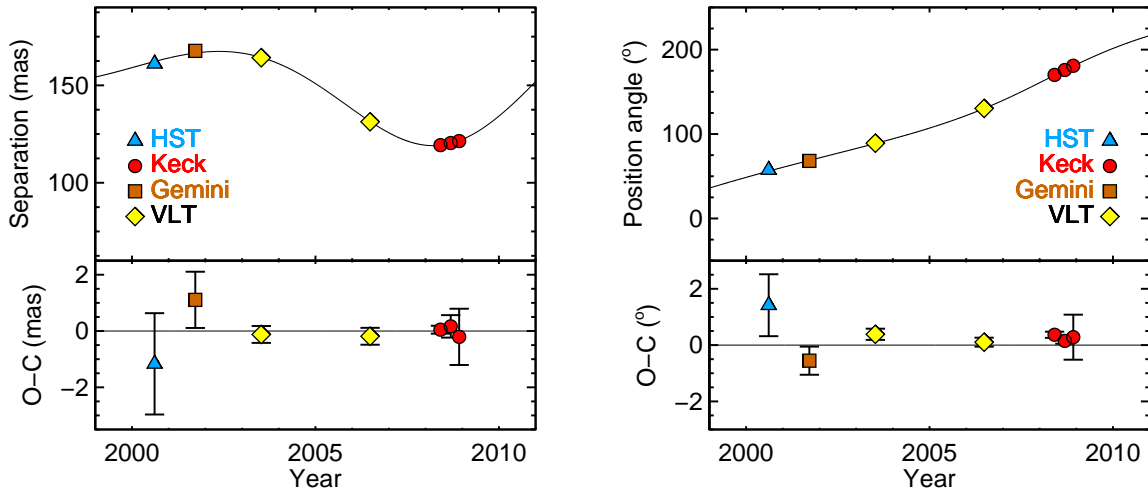


FIG. 3.— Measurements of the projected separation (*left*) and P.A. (*right*) of 2MASS J2206–2047AB. The best-fit orbit is shown as a solid line. The bottom panels show the observed minus predicted measurements with observational error bars.

we were unable to assess any additional systematic errors in the VLT astrometry by fitting simulated binary images. However, in our previous work we have found that the rms scatter among dithered VLT images has been a good representation of errors derived from such simulations (Dupuy et al. 2009b).

3. RESULTS

3.1. Orbit Determination and Dynamical Mass

Our observations together with archival data span 8.3 years of the orbit of 2MASS J2206–2047AB. We used a Markov Chain Monte Carlo (MCMC) approach, described in detail by Liu et al. (2008), to determine the probability distributions of all orbital parameters. Chains all had lengths of 2×10^8 steps, and the correlation length of our most correlated chain, as defined by Tegmark et al. (2004), was 5.4×10^4 for the orbital period. This gives an effective length of the chain of 3.7×10^3 , which in turn gives statistical uncertainties in the parameter errors of about $1/\sqrt{3.7 \times 10^3} = 1.6\%$, i.e., negligible. The single best-fit orbit has a reduced χ^2 of 1.07 (7 degrees of freedom) and is shown in Figures 2 and 3, and the best-fit parameters and their confidence limits are given in Table 4.

Applying Kepler’s Third Law ($M_{\text{tot}} = a^3/P^2$) to the period and semimajor axis distributions gives the posterior probability distribution for the total mass of 2MASS J2206–2047AB, which has a median of $0.152 M_{\odot}$, a standard deviation of $0.003 M_{\odot}$, and 68.3(95.4)% confidence limits of $^{+0.003}_{-0.003} (^{+0.007}_{-0.006}) M_{\odot}$ (Figure 4). The resulting MCMC probability distributions for all parameters are shown in Figure 5. It is evident from Figure 6 that the tight correlation between the two parameters P and a is responsible for the very precise total mass (2%), despite the fact the parameters are not independently determined as precisely (16% and 12%, respectively). The MCMC probability distribution of the total mass does not include the uncertainty in the parallax (9.1%), which by simple propagation of errors would contribute an additional $^{+32}_{-22}\%$ uncertainty in the mass. We account for this additional error by randomly drawing a normally distributed parallax value for each step

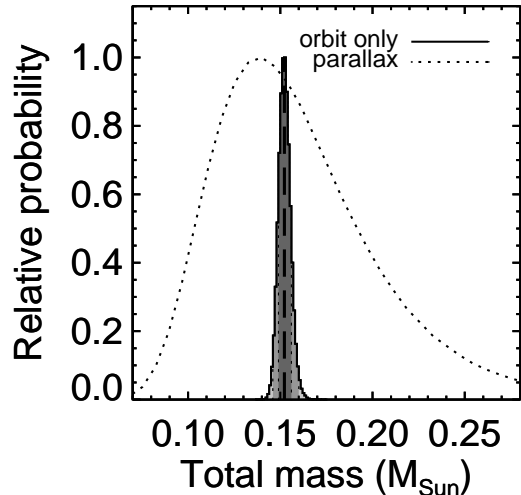


FIG. 4.— Probability distribution of the total mass of 2MASS J2206–2047AB resulting from our MCMC analysis. The histogram is shaded to indicate the 68.3%, 95.4%, and 99.7% confidence regions, which correspond to 1σ , 2σ , and 3σ for a normal distribution. The dashed line represents the median value of $0.152 M_{\odot}$. The standard deviation of the distribution is $0.003 M_{\odot}$. The dotted unshaded curve shows the final mass distribution after accounting for the additional $^{+32}_{-22}\%$ error due to the uncertainty in the parallax. The asymmetry in this curve is due to the asymmetric distance errors resulting from symmetric parallax errors. The confidence limits for both distributions are given in Table 4.

in the chain. The resulting mass distribution is asymmetric, and our final determination of the total mass is $0.15^{+0.05}_{-0.03} (^{+0.13}_{-0.06}) M_{\odot}$ at 68.3(95.4)% confidence.

As an independent verification of our MCMC results, we also fit the orbit of 2MASS J2206–2047AB using the linearized least-squares routine ORBIT (described in Forveille et al. 1999). All of the orbital parameters are consistent between the ORBIT and MCMC results, and

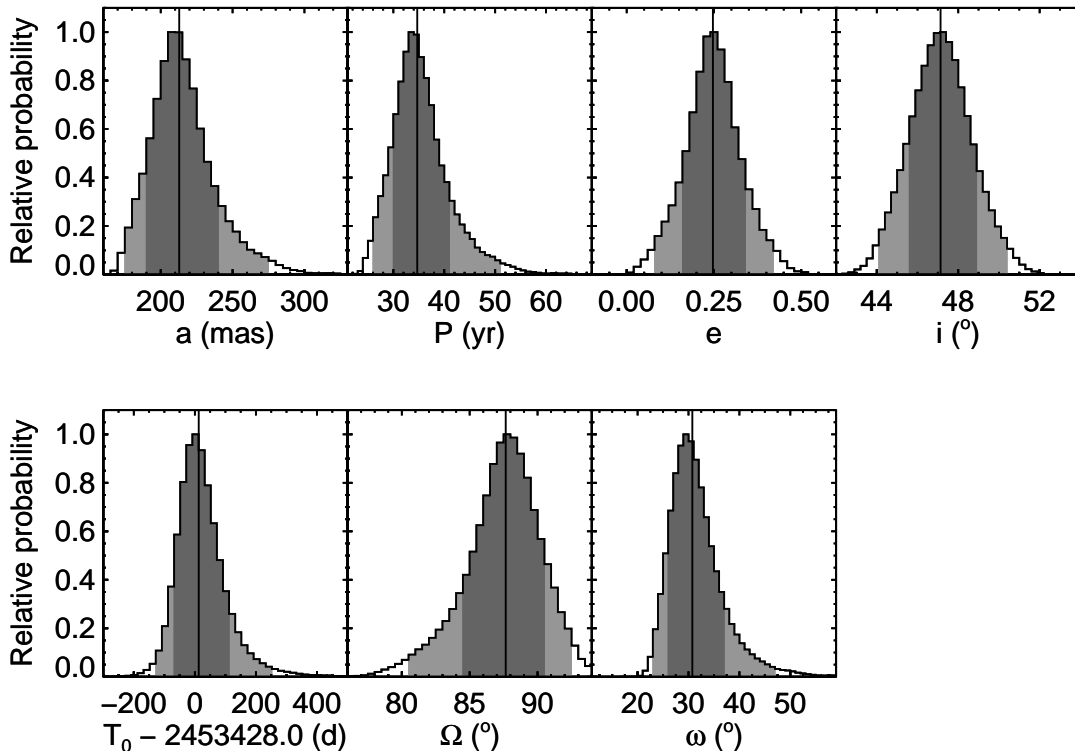


FIG. 5.— Probability distributions of all orbital parameters derived from the MCMC analysis: semimajor axis (a), orbital period (P), eccentricity (e), inclination (i), epoch of periastron (T_0), P.A. of the ascending node (Ω), and argument of periastron (ω). Each histogram is shaded to indicate the 68.3% and 95.4% confidence regions, which correspond to 1σ and 2σ for a normal distribution, and the solid vertical lines represent the median values. Note that T_0 is shown in days since UT 2005 March 11 00:00 for clarity.

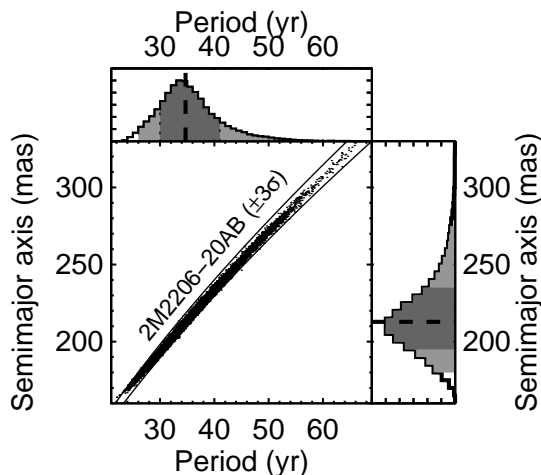


FIG. 6.— Steps in the MCMC chain show a high level of correlation between the orbital period and semimajor axis. This correlation enables the total mass to be determined more precisely than from simple propagation of errors for these two parameters ($M_{\text{tot}} = a^3/P^2$). Lines are drawn demarcating the 3σ range for the total mass of 2MASS J2206–2047AB without accounting for the distance uncertainty ($0.143\text{--}0.163 M_{\odot}$).

the resulting total mass and χ^2 were identical. Using ORBIT, we tested whether varying the input astrometry and corresponding uncertainties affected the orbital solution. We tried a variety of permutations: using the pub-

lished *HST* and/or Gemini astrometry (rather than our own); using Keck astrometry with and without Monte Carlo offsets and with rms or Monte Carlo-derived errors; and excluding one of the two VLT epochs. The resulting orbits had masses of $0.145\text{--}0.157 M_{\odot}$, with errors of $0.003\text{--}0.020 M_{\odot}$, and χ^2 of 1.07–2.32. Thus, the dynamical mass and corresponding error are not significantly impacted by the input astrometry, as all variation is much smaller than the parallax error, and our default solution has a lower χ^2 and mass uncertainty than any other plausible trial permutation.

3.2. Spectral Types

Using the integrated-light optical spectrum of 2MASS J2206–2047, both Gizis et al. (2000) and Crifo et al. (2005) found a spectral type of $M8.0 \pm 0.5$. Without resolved spectroscopy of the binary, we cannot directly determine the spectral types of the two components; however, our resolved photometry shows that they are nearly identical. To quantify the potential difference in spectral types, we compiled 2MASS photometry for the single M8.0, M8.5, and M9.0 objects with parallaxes from Monet et al. (1992) and Dahn et al. (2002). Between the spectral types M8.0 and M8.5, we found a difference in absolute magnitude of $\Delta M_J = 0.67 \pm 0.19$ mag, $\Delta M_H = 0.68 \pm 0.20$ mag, and $\Delta M_{K_S} = 0.64 \pm 0.22$ mag, where the uncertainty is the rms of objects in each bin added in quadrature. Between spectral types M8.0 and M9.0 we found only slightly larger magnitude differences. Our best measurement of the flux

TABLE 4
 DERIVED ORBITAL PARAMETERS FOR 2MASS J2206–2047AB

Parameter	MCMC			ORBIT ^a
	Median	68.3% c.l.	95.4% c.l.	
Semimajor axis a (mas)	213	–18, 24	–35, 60	210±30
Orbital period P (yr)	35	–5, 6	–9, 16	35±8
Eccentricity e	0.25	–0.08, 0.08	–0.17, 0.17	0.24±0.12
Inclination i (°)	47.1	–1.5, 1.6	–3, 3	47±2
Time of periastron passage $T_0 - 2453440.5^b$ (JD)	0	–60, 80	–130, 240	–1±80
P.A. of the ascending node Ω (°)	88	–3, 2	–7, 5	88±4
Argument of periastron ω (°)	31	–4, 6	–7, 16	31±6
Total mass (M_\odot): fitted ^c	0.152	–0.003, 0.003	–0.006, 0.007	0.152±0.003
Total mass (M_\odot): final ^d	0.15	–0.03, 0.05	–0.06, 0.13	0.15±0.04
Reduced χ^2 (7 degrees of freedom)	1.07	1.07

^aThe orbital parameters determined by ORBIT with their linearized 1σ errors.

^bUT 2005 March 11 00:00:00.0

^cThe “fitted” total mass represents the direct results from fitting the observed orbital motion without accounting for the parallax error. For the linearized ORBIT error, the covariance between P and a was taken into account.

^dThe “final” total mass includes the additional $^{+32}_{-22}\%$ error in the mass due to the error in the parallax.

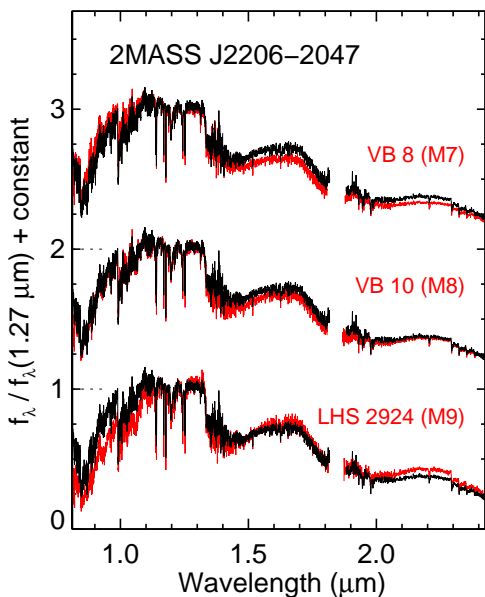


FIG. 7.— The integrated-light near-infrared spectrum of 2MASS J2206–2047 (black). Data for M dwarf spectral standards (red) are shown for comparison (Cushing et al. 2005). The best matching standard is VB 10 (M8), which is consistent with the optical spectral type of $M8.0\pm 0.5$ for 2MASS J2206–2047 (Gizis et al. 2000; Crifo et al. 2005).

ratio of 2MASS J2206–2047AB in each of these bands is $\Delta J = 0.06\pm 0.02$ mag, $\Delta H = 0.065\pm 0.017$ mag, $\Delta K_S = 0.067\pm 0.010$ mag.⁴ Thus, we find that the J , H , and K_s band photometry is inconsistent with the two components of 2MASS J2206–2047AB having different spectral types at 3.0σ , 3.1σ , and 2.6σ , respectively. Therefore, we

⁴ Note that our flux ratios in the J and H bands are actually determined using MKO filters, but we neglect the slight differences in the 2MASS and MKO photometric systems for this comparison.

adopt spectral types of $M8.0\pm 0.5$ for both components.

3.3. Bolometric Luminosities

Because of the identical spectral types and colors of the components of 2MASS J2206–2047AB, we computed their individual bolometric luminosities simply from the flux ratio and integrated-light bolometric luminosity. For the former, we used the most precise flux ratio available, which was 0.067 ± 0.010 mag from our 2008 September Keck K_S band data. There is no published value for the bolometric luminosity of 2MASS J2206–2047, so we computed it from its near-infrared spectrum and estimated L' band photometry. We obtained the spectrum on UT 2008 July 6 using IRTF/SpEx (Rayner et al. 2003) in SXD mode, which has five orders spanning $0.81\text{--}2.42\ \mu\text{m}$ ($R = 1200$). We calibrated, extracted, and telluric-corrected the data using the SpeXtool software package (Vacca et al. 2003; Cushing et al. 2004). In Figure 7 we show our spectrum alongside spectra from Cushing et al. (2005) of the M dwarf spectral standards defined by Kirkpatrick et al. (1991). As expected from the $M8.0\pm 0.5$ optical spectral type of 2MASS J2206–2047, the best matching standard is the M8 dwarf VB 10. To estimate the L' band photometry, we compiled the $K-L'$ colors of M dwarfs and early L dwarfs from Golimowski et al. (2004), which essentially follow a linear relation with spectral type. Fitting all single M1–L1 objects (i.e., excluding the binaries LHS 333AB, LHS 2397aAB, and 2MASS J0746+2000AB) and weighting by their photometric errors, we found

$$K_{\text{MKO}} - L' = 0.111 + 0.0526 \times \text{SpT} \quad (1)$$

where $K - L'$ is in mag, spectral type (SpT) is defined such that M0 = 0 and L0 = 10, and the rms about the fit was 0.07 mag. From this relation, we estimated a $K - L'$ color for 2MASS J2206–2047 of 0.53 ± 0.07 mag, resulting in an L' band magnitude of 10.73 ± 0.08 mag.⁵

⁵ We converted the 2MASS K_S band integrated-light photometry to the MKO photometric system using synthetic photometry of our SpeX spectrum: $K_{\text{MKO}} - K_{2\text{MASS}} = -0.051$ mag.

To derive the integrated-light bolometric luminosity, we numerically integrated our SpeX spectrum and the L' band photometric point at $3.8 \mu\text{m}$, interpolating between the gaps in the data, neglecting flux at shorter wavelengths, and extrapolating beyond L' band assuming a blackbody. We determined the luminosity error in a Monte Carlo fashion by adding randomly drawn noise to our data over many trials and computing the rms of the resulting luminosities. We accounted both for the noise in the spectrum and the errors in the 2MASS photometry used to flux-calibrate it. Before accounting for the error in the distance we found a total bolometric luminosity of $\log(L_{\text{bol}}/L_{\odot}) = -2.982 \pm 0.006$ dex. After accounting for this error, the symmetric parallax uncertainty results in slightly asymmetric luminosity errors, giving $\log(L_{\text{bol}}/L_{\odot}) = -2.98^{+0.08}_{-0.07}$ dex. Using the flux ratio to apportion this luminosity to the two binary components results in individual luminosities of $-3.27^{+0.08}_{-0.07}$ dex and $-3.30^{+0.08}_{-0.07}$ dex. In the following analysis, we correctly account for the covariance between these quantities (via the flux ratio), enabling more precise determinations of relative quantities (such as ΔT_{eff}) due to the more precise luminosity ratio ($\Delta \log(L_{\text{bol}}) = 0.027 \pm 0.004$ dex).

3.4. Atmospheric Model Fitting: T_{eff} , $\log(g)$, and R

Because the two components of 2MASS J2206–2047AB have essentially identical fluxes and colors, we can determine the effective temperatures and surface gravities of both by fitting atmospheric models to its integrated-light spectrum.⁶ We used the PHOENIX-Gaia (Brott & Hauschildt 2005) and the Ames-Dusty (Allard et al. 2001) solar-metallicity atmospheric models to fit our IRTF/SpeX SXD spectrum of 2MASS J2206–2047. The PHOENIX-Gaia models include updated line lists compared to the AMES-Dusty models, but they do not include the effects of dust. The treatment of dust in the Ames-Dusty models is an extreme limiting case (no dust settling), but models with a more sophisticated treatment of dust are not yet publicly available. For the PHOENIX-Gaia models, we used grids of synthetic spectra ranging in T_{eff} from 2000 to 3500 K ($\Delta T_{\text{eff}} = 100$ K) and $\log(g)$ from 3.5 to 5.5 ($\Delta \log(g) = 0.5$). For the Ames-Dusty models, we used grids of synthetic spectra ranging in T_{eff} from 1500 to 3400 K ($\Delta T_{\text{eff}} = 100$ K) and $\log(g)$ from 4.0 to 6.0 ($\Delta \log(g) = 0.5$).

Our fitting procedure utilized a Monte Carlo approach based on that of Cushing et al. (2008) and Bowler, Liu & Cushing (2009, submitted). To account for the heterogeneous resolution of our SXD spectrum, we Gaussian smoothed synthetic spectra in separate spectral ranges corresponding to the different SXD orders. When fitting our near-infrared spectrum ($0.81\text{--}2.42 \mu\text{m}$), we excluded a small region from $1.82\text{--}1.88 \mu\text{m}$ not covered by the instrument. We flux-calibrated our observed spectrum using 2MASS J , H , and K_S photometry. For each Monte Carlo trial, we applied small flux shifts to the observed spectrum corresponding to the spectroscopic

⁶ In Section 4.3, we use the measured total mass and luminosity ratio to derive from evolutionary models an effective temperature difference of 27 ± 5 K between the two components. Since the model grid steps are 100 K, a single-temperature fit to the integrated-light spectrum is valid.

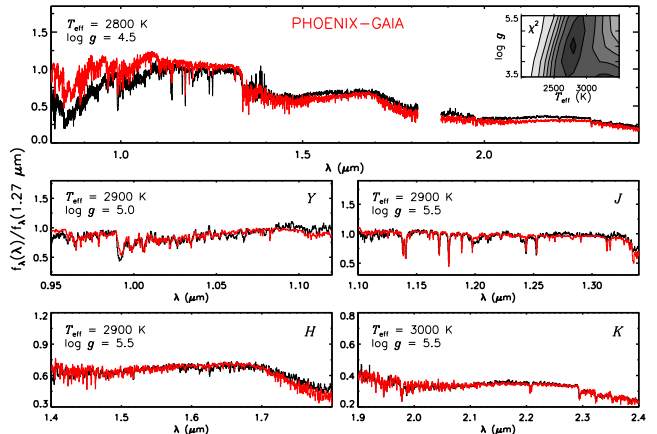


FIG. 8.— The integrated-light near-infrared spectrum of 2MASS J2206–2047 (black) shown with the best fitting PHOENIX-Gaia models (red) for the entire spectrum (top) and for individual spectral ranges (Y , J , H , and K bands). The top panel inset (upper right) shows χ^2 contours of 1.02, 1.1, 1.3, 1.5, 1.7, 2.0, 2.3, and 3.3 times the minimum χ^2 for model atmospheres compared to the entire spectrum. The model fit is well-constrained in T_{eff} and less so in $\log(g)$.

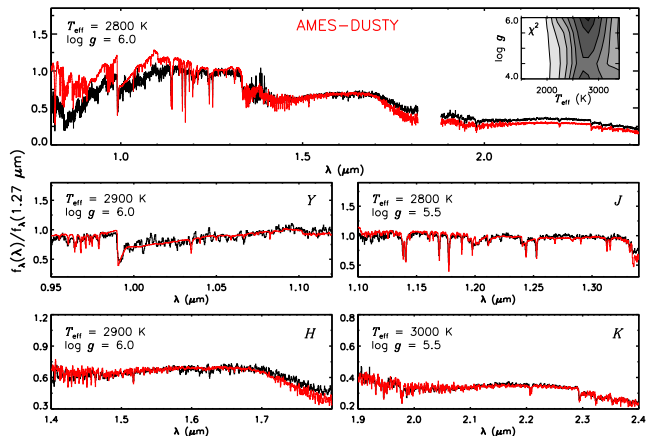


FIG. 9.— The integrated-light near-infrared spectrum of 2MASS J2206–2047 (black) shown with the best fitting Ames-Dusty models (red) for the entire spectrum (top) and for individual spectral ranges (Y , J , H , and K bands). The top panel inset (upper right) shows χ^2 contours of 1.02, 1.1, 1.3, 1.5, 1.7, 2.0, 2.3, and 3.3 times the minimum χ^2 for model atmospheres compared to the entire spectrum. The model fit is well-constrained in T_{eff} and that the minimum χ^2 is only achieved when the model $\log(g)$ reaches the upper limit of the grid.

(SpeX) and photometric (2MASS) measurement errors and then found the best fitting model by minimizing the χ^2 statistic. This process was repeated 10^3 times, after which we tallied the fraction of times each model yielded the best fit (f_{MC}). Fractions near 1.0 indicate that only a single model fit the data well. The results of our fitting procedure are given in Table 5, and the best-fit spectra for each set of models are shown in Figures 8 and 9.

Both sets of models gave best-fit effective temperatures

TABLE 5
BEST-FIT ATMOSPHERIC MODELS OF
2MASS J2206–2047AB

Spectral range	T_{eff} (K)	$\log(g)$	f_{MC}^{a}
PHOENIX-Gaia (Brott & Hauschildt 2005)			
All (0.81–2.42 μm)	2800	4.5	0.46
	2700	4.0	0.27
	3400	3.5 ^b	0.19
Y (0.95–1.12 μm)	2900	5.0	1.00
J (1.10–1.34 μm)	2900	5.5 ^b	0.99
H (1.40–1.80 μm)	2900	5.5 ^b	1.00
K (1.90–2.40 μm)	3000	5.5 ^b	1.00
Ames-Dusty (Allard et al. 2001)			
All (0.81–2.42 μm)	2800	6.0 ^b	0.99
Y (0.95–1.12 μm)	2900	6.0 ^b	0.54
	2800	5.5	0.46
J (1.10–1.34 μm)	2800	5.5	1.00
H (1.40–1.80 μm)	2900	6.0 ^b	0.95
K (1.90–2.40 μm)	3000	5.5	0.63
	3000	6.0 ^b	0.37

^aFraction of Monte Carlo trials in which the model gave the best fit.

^bThe best-fit value is at the edge of the model grid.

of 2800 K, but the best-fit PHOENIX-Gaia model had a lower surface gravity ($\log(g) = 4.5$) than the Ames-Dusty model ($\log(g) = 6.0$; the grid maximum). Although the f_{MC} value for the best-fit PHOENIX-Gaia model was only 0.46, the next best-fit model ($f_{\text{MC}} = 0.27$) had a temperature and gravity different by only one grid step ($T_{\text{eff}} = 2700$ K, $\log(g) = 4.0$). We also fitted the observed spectrum separately over individual bandpasses (Y, J, H, and K), and these fits yielded similar results to the entire spectrum, typically within 100 K and 0.5 dex (i.e., one model grid step). Thus, we adopt errors of ± 100 K and ± 0.5 dex on the best-fit parameters in order to account for the impact of the measurement errors on the fit as well as uncertainties in modeling a limited spectral range.

In addition to the effective temperature and surface gravity, the radius can be derived from atmospheric model fitting when the distance is known. This is because the scaling factor used to shift the synthetic spectrum to the observed flux-calibrated spectrum is a free parameter equal to R^2/d^2 . Accounting for the flux ratio between the two components, the error in the distance, and the rms scatter in this scaling factor over the 10^3 trials, we found identical radii of $0.096 \pm 0.009 R_{\odot}$ from the PHOENIX-Gaia models and $0.095 \pm 0.009 R_{\odot}$ from the Ames-Dusty models.⁷

3.5. Age Constraints from Kinematics and Activity

In this section, we consider whether the space motion or activity of 2MASS J2206–2047 can provide useful constraints on the age of the system. There are

⁷ Because more than one PHOENIX-Gaia model fit the data well (see Table 5), we used only the best fitting model’s scaling factors when deriving radii.

three values of its radial velocity in the literature: (1) 16.3 ± 2.7 km s^{−1} derived by Reid et al. (2002) from cross-correlation of the optical spectrum with radial velocity standards; (2) 8.0 ± 2.0 km s^{−1} also from Reid et al. (2002) but derived from the central wavelength of the H α emission line; and (3) 10.8 ± 1.3 km s^{−1} derived by Guenther & Wuchterl (2003) using the central wavelengths of unspecified spectral lines. Reid et al. (2002) attributed the discrepancy between their two radial velocities to the fact that 2MASS J2206–2047 is a fast rotator ($v \sin i = 22$ km s^{−1}) with an asymmetric H α profile, confusing their estimate of the H α centroid. 2MASS J2206–2047’s binarity was unknown to Reid et al. (2002), and we note that this could be partially responsible for the discrepancy. For example, if one component dominated the H α emission, the H α centroid would be offset from the cross-correlation velocity (which likely represents the average velocity of the two components) by 1.8 km s^{−1}, assuming a mass ratio of unity. However, this alone is insufficient to account for the 8.3 km s^{−1} discrepancy observed.

We used the cross-correlation radial velocity (16.3 ± 2.7 km s^{−1}) from Reid et al. (2002) and the parallax and proper motion from Costa et al. (2006) to derive the heliocentric velocity of 2MASS J2206–2047: $(U, V, W) = (+7.8 \pm 1.6, +1.7 \pm 1.1, -15.0 \pm 2.1)$ km s^{−1}. We adopted the sign convention for U that is positive toward the Galactic center and accounted for the errors in the parallax, proper motion, and radial velocity in a Monte Carlo fashion. For comparison, we compiled all objects of spectral type M7 or later that have the radial velocities, parallaxes, and proper motions necessary for computing space motions (described in detail in Section 3.4 of Dupuy et al. 2009b). 2MASS J2206–2047 is only 1.3σ away from the mean of this population’s space motion ellipsoid (Figure 10). Thus, its space motion is not significantly different from other ultracool dwarfs, implying an age consistent with the population of ultracool dwarfs as a whole. Several authors have attempted to estimate the age of this population, typically comparing the distribution of tangential velocities (V_{tan} , which requires only a proper motion and distance determination) to the well studied nearby populations of FGKM stars. The resulting age for the population of ultracool dwarfs estimated in this way has been found to be 2–4 Gyr (Dahn et al. 2002; Faherty et al. 2009).⁸

We have also assessed 2MASS J2206–2047’s membership in the Galactic populations of the thin disk (1–10 Gyr; e.g., Wood & Oswald 1998) and thick disk (~ 10 Gyr; e.g., Ibukiyama & Arimoto 2002) using the Besançon model of the Galaxy (Robin et al. 2003). Our method is described in Section 3.4 of our study of LHS 2397a (Dupuy et al. 2009b), and for 2MASS J2206–2047 we found a membership probability of $> 99.9\%$ for the thin disk and $< 0.1\%$ for the thick disk.

Finally, the fact that 2MASS J2206–2047 is chromo-

⁸ Zapatero Osorio et al. (2007) determined a somewhat younger age (~ 1 Gyr) for the population of ultracool dwarfs, based on the small sample of L and T dwarfs with full space velocities (21 objects). However, since L and T dwarfs span a wider range of masses than earlier type objects, a typical IMF that rises at lower masses will naturally increase the number of young objects in this sample, biasing a kinematically derived age (e.g., see Section 4.5 of Dahn et al. 2002).

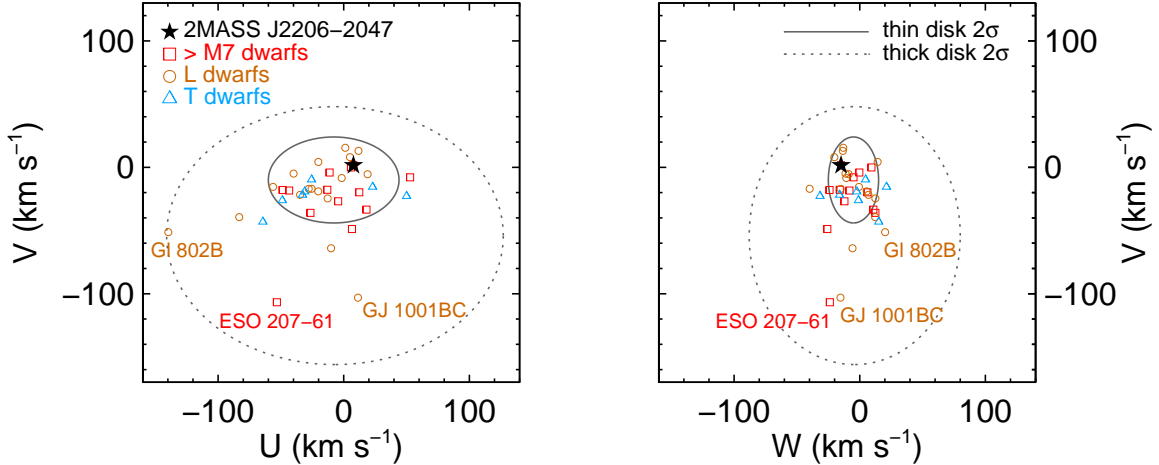


FIG. 10.— The heliocentric space velocity of 2MASS J2206–2047 (star) shown alongside other ultracool dwarfs: $> M7$ dwarfs (squares), L dwarfs (circles), and T dwarfs (triangles). The 2σ ellipsoids of the thin disk (solid line) and thick disk (dotted line) as predicted by the Besançon galaxy model (Robin et al. 2003) are also shown for comparison. The space velocity of 2MASS J2206–2047 is consistent with other ultracool dwarfs, and we derive a $> 99.9\%$ thin disk membership probability.

spherically active ($\log(L_{\text{H}\alpha}/L_{\text{bol}}) = -4.59, -4.54$; Gizis et al. 2000; Reid et al. 2002, respectively) could also potentially provide an age constraint, as the activity of M dwarfs changes with age. West et al. (2008) showed that the fraction of active M dwarfs as a function of the vertical distance above the Galactic plane (z) provides a constraint on the activity lifetime of M dwarfs, given a model of how thick disk heating pumps up z over time. West et al. (2008) found that the activity lifetime increases monotonically with M dwarf spectral type, and the latest type for which they were able to determine a robust lifetime was M7 ($8.0^{+0.5}_{-1.0}$ Gyr). This provides a weak constraint on the age of 2MASS J2206–2047, as its activity is therefore expected to last for at least $\gtrsim 8$ Gyr.

4. TESTS OF MODELS

Our measured total mass of 2MASS J2206–2047AB enables strong tests of theoretical models, and in the following analysis we consider two independent sets of evolutionary models: the Tucson models (Burrows et al. 1997) and the Lyon Dusty models (Chabrier et al. 2000). Our approach follows previous work for 2MASS J1534–2952AB (Liu et al. 2008), HD 130948BC (Dupuy et al. 2009a), and LHS 2397aAB (Dupuy et al. 2009b). We drew measured properties (summarized in Table 6) from random distributions, carefully accounting for the covariance between different quantities (e.g., M_{tot} and L_{bol} are correlated through the distance), and we used L_{bol} (rather than T_{eff}) as the basis for our model comparisons.

4.1. Model-Inferred Age

As described in detail by Liu et al. (2008) and Dupuy et al. (2009a), the total mass of a binary along with its individual component luminosities can be used to estimate the age of the system from evolutionary models. This age estimate can be surprisingly precise when both components are likely to be substellar since their luminosities depend very sensitively on age. However, with spectral types of $M8.0 \pm 0.5$, both components of 2MASS J2206–2047AB are likely to be stars unless the

system is quite young.

We derived an age of $0.4^{+9.6}_{-0.2}$ Gyr from both the Tucson and Lyon models (Figure 11). Because the median total mass is $0.15 M_{\odot}$, which is roughly the limit at which both components would be brown dwarfs, the median age derived from models is correspondingly young. However, the 1σ uncertainty in the total mass reaches $0.20 M_{\odot}$, in which case both components would be main-sequence stars. In this case, since stars do not dim over time as brown dwarfs do, the luminosities of both components do

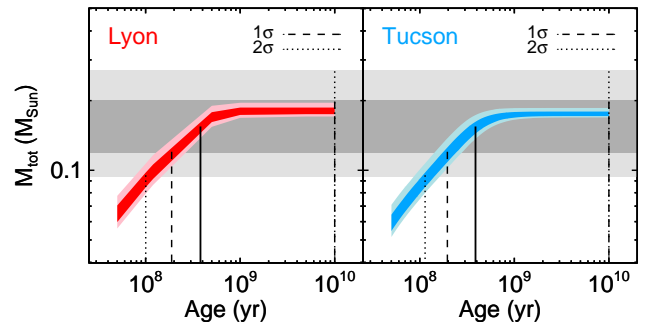


FIG. 11.— Total mass (M_{tot}) predicted by evolutionary models as a function of age, given the observational constraint of the luminosities of the two components of 2MASS J2206–2047AB. The curved shaded regions show the 1σ and 2σ ranges in this model-derived mass. By applying the additional constraint of the measured total mass (M_{tot}), we used the models to determine the age of 2MASS J2206–2047AB (see Section 4.1). The horizontal gray bars show our 1σ and 2σ constraints on the total mass, and the resulting median, 1σ , and 2σ model-inferred ages are shown by solid, dashed, and dotted lines, respectively. Model-inferred ages are truncated at 10 Gyr (the oldest age included in both sets of models), which happens at 1σ for both models. Note that the upper limit of the M_{tot} distribution corresponds to both components of 2MASS J2206–2047AB being stars, and evolutionary models do not reach faint enough luminosities for such high mass objects at any age.

TABLE 6
 MEASURED PROPERTIES OF 2MASS J2206–2047AB

Property ^a	Component A	Component B	Ref.
$M_{\text{tot}} (M_{\odot})$	$0.15^{+0.05}_{-0.03}$		1
Semimajor axis (AU)	$5.8^{+0.8}_{-0.7}$		1,2
d (pc)	$26.7^{+2.6}_{-2.1}$		2
Spectral type	$M8.0 \pm 0.5$	$M8.0 \pm 0.5$	1,3
T_{eff} (K)	2800 ± 100^b	2800 ± 100^b	1
J (mag)	13.07 ± 0.02	13.13 ± 0.02	1,4
H (mag)	12.44 ± 0.02	12.51 ± 0.02	1,4
K (mag)	11.98 ± 0.03	12.05 ± 0.03	1,4
$J - H$ (mag)	0.63 ± 0.03	0.62 ± 0.03	1,4
$H - K$ (mag)	0.46 ± 0.04	0.45 ± 0.04	1,4
$J - K$ (mag)	1.08 ± 0.04	1.08 ± 0.04	1,4
M_J (mag)	10.93 ± 0.19	$10.99^{+0.19}_{-0.20}$	1,2,4
M_H (mag)	$10.31^{+0.18}_{-0.20}$	$10.38^{+0.18}_{-0.20}$	1,2,4
M_K (mag)	$9.86^{+0.18}_{-0.20}$	$9.92^{+0.18}_{-0.20}$	1,2,4
$\log(L_{\text{bol}}/L_{\odot})$	$-3.27^{+0.08}_{-0.07}$	$-3.30^{+0.08}_{-0.07}$	1,2
$\Delta \log(L_{\text{bol}})$	0.027 ± 0.004		1

REFERENCES. — (1) This work; (2) Costa et al. (2006); (3) Gizis et al. (2000); Crifo et al. (2005); (4) Cutri et al. (2003).

^aAll near-infrared photometry on the MKO system.

^bBased on spectral synthesis model fitting.

not strongly constrain the age of the system. Thus, while the lower bound of our uncertainty on the model-derived age corresponds to the age a pair of brown dwarfs would need to be to match the observed luminosities and total mass, the upper limit is essentially unconstrained. Our limit of 10 Gyr comes from the fact that the evolutionary models are computed only up to this age. In our analysis, which uses a Monte Carlo approach to compute model-derived properties, we found that about 30% of the time the randomly drawn observed luminosities were too low to match the randomly drawn total mass. In other words, models would never predict that such massive objects ($\gtrsim 0.09 M_{\odot}$ stars) could be as faint as the components of 2MASS J2206–2047AB, and in such cases we assigned an age of 10 Gyr.

4.2. Individual Masses

Given the near unity flux ratio of 2MASS J2206–2047AB, we expect the mass ratio to also be very close to unity. We used evolutionary models to estimate the mass ratio of 2MASS J2206–2047AB ($q \equiv M_B/M_A$) by constraining the model-derived individual masses of 2MASS J2206–2047A and 2MASS J2206–2047B to add up to the observed total mass, while still matching their observed luminosities. The Tucson models gave $q = 0.981^{+0.012}_{-0.007}$, while the Lyon models gave a consistent value of $0.982^{+0.008}_{-0.006}$. The resulting individual masses (Table 7) are essentially identical to those resulting from an assumed mass ratio of unity, with the exception of the upper confidence limits. This is due to the effect described in Section 4.1 where about 30% of the randomly drawn total masses and individual luminosities were inconsistent with any models. In these cases, we assigned the highest individual masses for which the luminosities were consistent with the models. In Section 5.1, we consider the issue of plausible individual masses in more detail.

 TABLE 7
 EVOLUTIONARY MODEL-DERIVED PROPERTIES OF
 2MASS J2206–2047AB

Property	Median	68.3% c.l.	95.4% c.l.
Tucson Models (Burrows et al. 1997)			
System			
Age (Gyr) ^a	0.4	–0.2, 9.6	–0.3, 9.6
$q (M_B/M_A)$	0.981	–0.007, 0.012	–0.013, 0.014
ΔT_{eff} (K)	27	–5, 5	–9, 11
Component A			
$M_A (M_{\odot})$	0.077	–0.017, 0.010	–0.030, 0.014
$T_{\text{eff},A}$ (K)	2660	–100, 90	–190, 170
$\log(g_A)$ (cgs)	5.26	–0.17, 0.09	–0.33, 0.12
$R_A (R_{\odot})$	0.109	–0.006, 0.008	–0.010, 0.018
Li_A/Li_0	0.0	–0.0, 0.8	–0.0, 1.0
Component B			
$M_B (M_{\odot})$	0.076	–0.017, 0.011	–0.029, 0.015
$T_{\text{eff},B}$ (K)	2640	–100, 90	–200, 170
$\log(g_B)$ (cgs)	5.26	–0.17, 0.10	–0.33, 0.13
$R_B (R_{\odot})$	0.108	–0.006, 0.009	–0.010, 0.018
Li_B/Li_0	0.0	–0.0, 0.9	–0.0, 1.0
Lyon Models (Dusty; Chabrier et al. 2000)			
System			
Age (Gyr) ^a	0.4	–0.2, 9.6	–0.3, 9.6
$q (M_B/M_A)$	0.982	–0.006, 0.008	–0.012, 0.011
ΔT_{eff} (K)	27	–4, 5	–8, 9
Component A			
$M_A (M_{\odot})$	0.077	–0.017, 0.012	–0.030, 0.018
$T_{\text{eff},A}$ (K)	2550	–100, 90	–200, 170
$\log(g_A)$ (cgs)	5.17	–0.18, 0.12	–0.34, 0.13
$R_A (R_{\odot})$	0.119	–0.007, 0.010	–0.011, 0.021
Li_A/Li_0	0.2	–0.2, 0.5	–0.2, 0.8
Component B			
$M_B (M_{\odot})$	0.076	–0.017, 0.013	–0.029, 0.018
$T_{\text{eff},B}$ (K)	2530	–100, 90	–200, 170
$\log(g_B)$ (cgs)	5.17	–0.18, 0.12	–0.34, 0.14
$R_B (R_{\odot})$	0.118	–0.007, 0.010	–0.011, 0.021
Li_B/Li_0	0.2	–0.2, 0.5	–0.2, 0.8

^aBoth sets of evolutionary models are only computed up to an age of 10 Gyr; therefore, this defines the upper limit on the model-derived ages.

4.3. Temperatures and Surface Gravities

Without radius measurements for 2MASS J2206–2047A and 2MASS J2206–2047B, we cannot directly determine their effective temperatures or surface gravities.⁹ In Section 3.4 we derived these properties by fitting atmospheric model spectra to the integrated-light spectrum, and we have also used evolutionary models to estimate these properties in the same fashion as our model-derived age and individual masses. The Tucson models give effective temperatures for 2MASS J2206–2047A and 2MASS J2206–2047B of 2660^{+90}_{-100} K and 2640^{+90}_{-100} K and surface gravities of $5.26^{+0.09}_{-0.17}$ and $5.26^{+0.10}_{-0.17}$ (cgs). The Lyon models give systematically lower but formally consistent temperatures of 2550^{+90}_{-100} K and 2530^{+90}_{-100} K and surface

⁹ Since at least one component of 2MASS J2206–2047AB is chromospherically active, it may be possible to estimate one or both radii using the technique employed by Berger et al. (2009) who measured the rotation period of 2MASSW J0746425+200032A from its chromospheric radio emission and combined this with its $v \sin(i)$ and orbital inclination (i) to derive its radius. This method assumes that the orbital and rotation axes are aligned. With a $v \sin(i)$ of 22 km s^{-1} (Reid et al. 2002), the active component(s) of 2MASS J2206–2047AB is expected to have a rotation period of about 280 minutes.

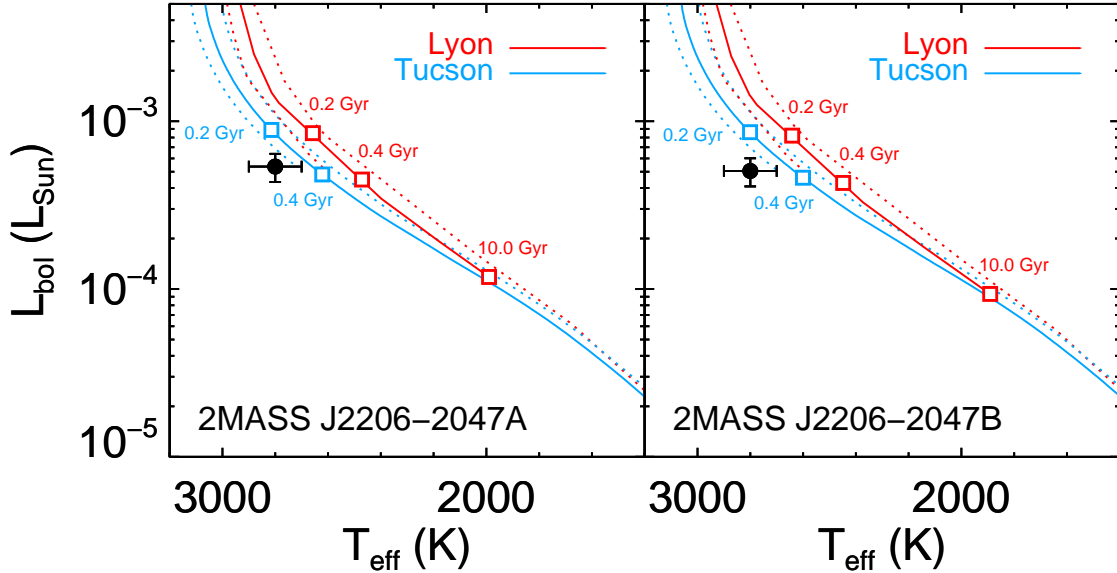


FIG. 12.— Hertzsprung-Russell diagram showing isomass lines from evolutionary models for the mass of 2MASS J2206–2047A (left) and 2MASS J2206–2047B (right) with dotted lines encompassing the 1σ mass uncertainties. The open squares demarcate the median and 1σ confidence limits on the evolutionary model-derived age of 2MASS J2206–2047AB. Our derived effective temperature from spectral synthesis fitting of the integrated light spectrum is shown as a filled circle with 100 K error bars. The atmospheric model temperature is warmer than both sets of evolutionary tracks but is only significantly discrepant with the Lyon model tracks.

gravities of $5.17^{+0.12}_{-0.18}$ and $5.17^{+0.12}_{-0.18}$ (cgs). (Note that the upper confidence limits are likely affected by the same truncation within our Monte Carlo method as discussed in Section 4.2 for the individual masses.) The differences between the two sets of models are due to the fact that the Tucson models predict radii that are 9% smaller than predicted by Lyon models (Table 7).

Compared to the effective temperature of 2800 ± 100 K derived from spectral synthesis fitting, the Tucson models are consistent (at 1.0 – 1.2σ), but the Lyon model temperatures are 1.9 – 2.0σ lower. This is illustrated in Figure 12, which shows the atmospheric model-derived temperatures in comparison to the evolutionary tracks on the Hertzsprung-Russell (H-R) diagram. As a result of this temperature discrepancy, the Tucson and Lyon model-predicted radii are larger than derived from the atmospheric model scaling factors by 14% and 24%, respectively. These could be brought into better agreement if the system were older than the median model-derived age of 0.4 Gyr, as evolutionary models would predict smaller radii and thus higher effective temperatures (corresponding to the 2σ lower/upper limits in Table 7 for radii/temperatures). Finally, atmospheric model fitting did not yield consistent surface gravity estimates: the dust-free PHOENIX-Gaia models gave $\log(g) = 4.5$, and the Ames-Dusty models gave $\log(g) = 6.0$ (the maximum allowed by the model grid). These are respectively lower and higher than the evolutionary model-derived surface gravities of $\log(g) = 5.0$ – 5.4 .

4.3.1. Comparison to Field Dwarfs

The model-derived effective temperatures for both components of 2MASS J2206–2047AB can be compared to those which have been determined for other objects of similar spectral type. Temperatures have been estimated in a number of ways, always relying to some degree on

models due to the lack of direct radius measurements, and we summarize such estimates for late-M dwarfs in order from most to least model dependent.

- *Spectral synthesis.* Fitting atmospheric models over a very narrow spectral range (2.297 – $2.310 \mu\text{m}$; $R = 42000$), Jones et al. (2005) found effective temperatures of 2900 K for the two M7–M9 dwarfs in their study. Using a broader spectral range (0.7 – $2.5 \mu\text{m}$; $R = 600$ – 3000), Leggett et al. (2001) found much cooler temperatures of 2100–2300 K for the five M7–M9 dwarfs in their study. Comparing our atmospheric model derived temperature of 2800 ± 100 K to these determinations, it is consistent with the former but > 400 K inconsistent with the latter. We investigated this discrepancy by using a similar spectral fitting approach as Leggett et al. (2001), which excludes the 1.5 – $1.7 \mu\text{m}$ portion of the spectrum, weights the spectral regions 0.7 – $1.4 \mu\text{m}$ and 2.0 – $2.5 \mu\text{m}$ by a factor of 5 higher than the rest of the spectrum, and finally selects the best fitting spectrum by eye. When we employed this procedure, we found an effective temperature of 2500 K for 2MASS J2206–2047, which is consistent with the Leggett et al. (2001) measurements of M7–M9 dwarfs (assuming 100 K uncertainties in both determinations).
- *Model radii.* For objects with L_{bol} measurements, the nearly flat mass–radius relationship predicted by theoretical models for very low-mass stars and brown dwarfs may be utilized to estimate T_{eff} . Adopting an age range of 0.1–10 Gyr, Leggett et al. (2001) derived effective temperatures of 1850–2650 K for the five M7–M9 dwarfs in their sample with L_{bol} measurements, and this broad range is

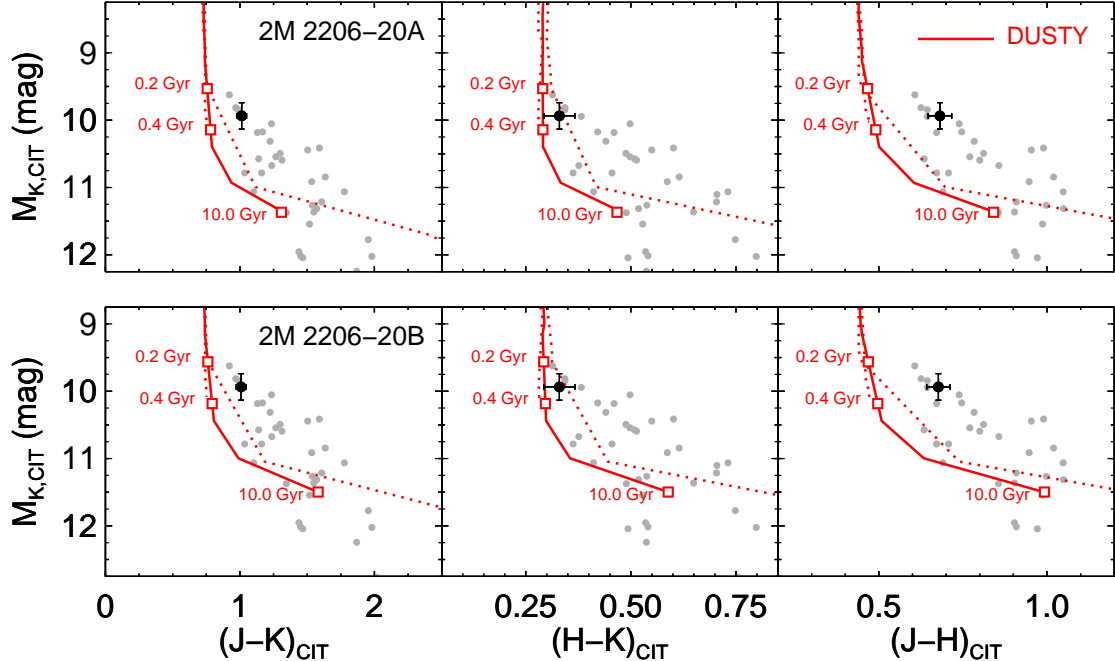


FIG. 13.— Color-magnitude diagrams showing the measured photometry of 2MASS J2206–2047A (top) and 2MASS J2206–2047B (bottom) compared to Lyon evolutionary tracks (JHK photometry on the CIT system). The solid lines are isomass tracks from the Dusty (Chabrier et al. 2000) models with dotted lines encompassing the 1σ mass uncertainties. The open squares demarcate the median and 1σ confidence limits on the evolutionary model-derived age of 2MASS J2206–2047AB. Field dwarfs with parallax measurements more precise than 10% and JHK colors more precise than 0.10 mag are shown as filled gray circles. Both components of 2MASS J2206–2047AB have identical colors and are typical of field dwarfs. However, evolutionary models do not reproduce the observed colors, with the exception of $H - K$.

consistent with our model-derived effective temperatures.

- *Mass benchmarks.* Objects in binaries with measured individual luminosities *and* a dynamical total mass enable more precise model-derived temperatures and gravities. This is the method we have used to determine the effective temperatures of both components of 2MASS J2206–2047AB, and Dupuy et al. (2009b) have previously used an identical method to determine the temperature and surface gravity of LHS 2397aA (M8.0±0.5): the Tucson models gave 2580 ± 30 K and $5.381^{+0.009}_{-0.014}$ (cgs), and the Lyon models gave 2470 ± 30 K and $5.307^{+0.007}_{-0.008}$ (cgs). These temperatures are consistent with those derived for 2MASS J2206–2047AB from evolutionary models, though LHS 2397aA is predicted to be 80 K cooler due to its slightly lower L_{bol} . Although an indirect comparison, we note that our atmospheric model temperature of 2800 ± 100 K is about 200–300 K higher than the evolutionary model derived temperature of LHS 2397aA. The evolutionary model-derived surface gravities of 2MASS J2206–2047AB are lower than LHS 2397aA and formally inconsistent; however, this is easily explained by the higher mass of LHS 2397aA (e.g., Tucson models give $0.0839^{+0.0007}_{-0.0015} M_{\odot}$).

- *Infrared flux method.* The infrared flux method

is a nearly model-independent way of estimating effective temperature that relies on a monochromatic flux measurement in the Rayleigh-Jeans tail of an SED as well as a bolometric flux measurement (Blackwell & Shallis 1977). Gautier et al. (2007) used their 24 μm *Spitzer*/MIPS photometry to determine effective temperatures for nine M7.5–M8.5 dwarfs by this method, finding temperatures of 2400–2730 K.¹⁰ These effective temperatures are in excellent agreement with the evolutionary model-derived temperatures for both components of 2MASS J2206–2047AB but somewhat lower (70–400 K) than the temperature from spectral synthesis fitting.

4.4. Near-Infrared Colors

The Lyon evolutionary models provide predictions of the fluxes of ultracool dwarfs in standard filter band-passes as a function of model mass and age.¹¹ We derived the model-predicted near-infrared colors of both components of 2MASS J2206–2047AB in the same fashion as the individual masses, effective temperatures, and age (i.e., using the combined observational constraints of the total mass and individual luminosities). Figure 13 shows

¹⁰ This range excludes the M8+L7 binary LHS 2397aAB as the companion flux likely contaminates the MIPS measurement (see discussion in Section 4.3.1 of Dupuy et al. 2009b).

¹¹ The models give JHK photometry on the CIT system, and we converted our photometry to this system using the relations of Carpenter (2001).

the observed colors of 2MASS J2206–2047AB on color–magnitude diagrams in comparison to model tracks and other field dwarfs. Compared to the observed colors of the components of 2MASS J2206–2047AB, only $H - K$ is consistent with the Dusty models, and both $J - K$ and $J - H$ are about 0.2–0.3 mag redder than predicted by Dusty. Since field M8 dwarfs have very similar colors to the components of 2MASS J2206–2047AB, the Lyon Dusty models will generally provide inaccurate estimates of the fundamental properties of late-M dwarfs from their near-infrared colors.

5. DISCUSSION

5.1. Additional Constraints on the Mass

We have directly measured the total mass of 2MASS J2206–2047AB to be $0.15^{+0.05}_{-0.03} M_{\odot}$. However, the entire range of formally allowed masses is not consistent with some of its other properties. For example, at the 1σ upper limit in M_{tot} , both components of 2MASS J2206–2047AB would be $0.10 M_{\odot}$ stars, but they would then be 0.7 mag fainter at K band than the faintest object of comparable mass (Gl 234B: $0.1034 \pm 0.0035 M_{\odot}$, $M_K = 9.26 \pm 0.04$; Delfosse et al. 2000; Ségransan et al. 2000). In contrast, the objects closest in K -band brightness to 2MASS J2206–2047AB are GJ 1245C ($0.074 \pm 0.013 M_{\odot}$, $M_K = 9.99 \pm 0.04$; Henry et al. 1999) and LHS 2397aA ($0.0848 \pm 0.0011 M_{\odot}$,¹² $M_K = 10.06 \pm 0.07$; Dupuy et al. 2009b). Thus, it is more likely that the components of 2MASS J2206–2047AB have individual masses in this range; in which case, the total mass would be well below the formally allowed value of $0.20 M_{\odot}$.

The 1σ lower limit of $M_{\text{tot}} = 0.12 M_{\odot}$ corresponds to a pair of $0.06 M_{\odot}$ brown dwarfs, and masses at or below this value are also disfavored. Reid et al. (2002) found an upper limit of 0.05 \AA for lithium absorption at 6807 \AA in the integrated-light spectrum of 2MASS J2206–2047, indicating that both components have depleted their initial lithium. As discussed by Chabrier et al. (1996), lithium can only be depleted in objects more massive than $\approx 0.06 M_{\odot}$. Moreover, even more massive objects require a finite amount of time to become lithium depleted: according to Chabrier et al. (1996), a $0.070 M_{\odot}$ object takes 0.2 Gyr to destroy 99% of its initial lithium, with lower mass objects taking longer. Given the constraint of the individual luminosities of 2MASS J2206–2047AB, the low-mass tail of the M_{tot} distribution corresponds to young ages. At the median mass of $0.15 M_{\odot}$ the model-derived age is 0.4 Gyr, and at the 1σ lower bound of $0.12 M_{\odot}$ the age is 0.2 Gyr. Below this 1σ limit, the components of 2MASS J2206–2047AB would be inconsistent with the lithium non-detection: (1) they would have had insufficient time to destroy their initial lithium, and/or (2) they should be low enough mass that they would never destroy any lithium. Thus, regardless of the precise location of the lithium-fusing boundary, the formally allowed low-mass tail of the M_{tot} distribution is not physically plausible.

5.2. Direct Measurement of the Mass Ratio

¹² Note that the mass of LHS 2397aA is derived from a total dynamical mass and evolutionary models.

Since the components of 2MASS J2206–2047AB are nearly identical, testing models using our measured total mass is straightforward. However, future measurements may constrain the binary’s mass ratio directly. Given that the flux ratio is so near unity, the mass ratio would not be feasible to measure from astrometric monitoring of the photocenter since the center-of-light would be imperceptibly different from the center-of-mass. Thus, the mass ratio must be determined through radial velocity monitoring. This is also challenging as the binary is currently approaching $\Delta V = 0 \text{ km s}^{-1}$ and will not reach the next peak in the radial velocity curve for $P/4 \approx 9$ years, in 2018. Until then, the radial velocities of the two components will remain below 1.4 km s^{-1} . Since the velocity of each component must be measured to 7% in order to determine the mass ratio to 10%, radial velocity measurements with a precision better than 0.1 km s^{-1} are needed. This is at the limit of state-of-the-art techniques using current instrumentation (Blake et al. 2007) but are well within reach of future near-infrared spectrographs with precision goals of 1 m s^{-1} (Jones et al. 2008).

6. CONCLUSIONS

We have determined the orbit of the M8+M8 binary 2MASS J2206–2047AB using relative astrometry spanning 8.3 years of its 35^{+6}_{-5} year orbit. The astrometry and corresponding errors used to derive this orbit were thoroughly examined through Monte Carlo simulations, using PSF reference sources for the AO images. The resulting best-fit orbit has a reduced χ^2 of 1.07 and total mass of $0.15^{+0.05}_{-0.03} M_{\odot}$. Because the orbit only contributes 2.0% to the mass error, the uncertainty in the dynamical mass is dominated by the 9.1% error in the parallax, which translates into an asymmetric $^{+32}_{-22}\%$ mass error. Although this mass is sufficiently precise to perform interesting model tests, a more precise parallax would provide even stronger tests and would remove the large ambiguity in the characterization of the system (i.e., whether it is composed of young brown dwarfs or old stars).

We have used evolutionary models to derive the properties of 2MASS J2206–2047AB using Monte Carlo methods developed in previous studies (e.g., Liu et al. 2008; Dupuy et al. 2009a). Both the Tucson and Lyon Dusty models give an age for the system of $0.4^{+9.6}_{-0.2}$ Gyr. The median age is somewhat young because the median total mass is somewhat low given the individual luminosities; however, the 1σ upper bound extends to the maximum allowed age (10 Gyr). This model-derived age is consistent with 2MASS J2206–2047’s space motion and its chromospheric activity.

We also derived the near-infrared colors of both components of 2MASS J2206–2047AB from the Lyon models and compared them to our observations. We found that the model $J - H$ and $J - K$ colors were significantly (0.2–0.3 mag) bluer than observed, while the model $H - K$ colors were in good agreement, suggestive of an important opacity source missing at J band in the Dusty models (or else systematic errors that cancel out for $H - K$). In any case, our observations show that masses and/or ages derived from the Dusty evolutionary models on the color–magnitude diagram will be in error for objects such as 2MASS J2206–2047AB.

Our effective temperature determinations from evolutionary models are in very good agreement with T_{eff} de-

terminations for other M7.5–M8.5 dwarfs: (1) from the infrared flux method (Gautier et al. 2007), and (2) from a similar mass benchmark system including the M8 dwarf LHS 2397aA (Dupuy et al. 2009b). We also derived effective temperatures for both components from atmospheric model fitting of the integrated-light spectrum, which is made possible by their essentially identical fluxes and colors. We found that these temperatures (2800 ± 100 K) are warmer than predicted by evolutionary models and are most discrepant (2σ) with the Lyon Dusty models (n.b., the surface boundary condition for the Lyon evolutionary models is determined by the same Dusty atmospheric models as we used for spectral synthesis fitting). This modest discrepancy may be caused by systematic errors in the atmospheric models, which use a maximal limiting case in the treatment of dust and incomplete line lists. Alternatively, the discrepancy could be explained if the system were somewhat older than the median age of 0.4 Gyr inferred from its luminosity and mass, as this would cause evolutionary model radii to be smaller and the derived effective temperatures warmer. In such a scenario, the true mass would be in the high-mass tail of the M_{tot} distribution, corresponding to a larger distance to the system, which can be tested directly with an improved parallax measurement.

Stars at the bottom of the main sequence experience much of the same atmospheric physics as the warmest brown dwarfs and extrasolar planets because of the presence of dust in their photospheres. The characterization of such objects largely relies on theoretical models that must accurately describe the behavior of this dust as well as the opacity due to millions of molecular transitions (e.g., Barber et al. 2006). Dynamical mass measurements for ultracool binaries like 2MASS J2206–2047AB provide the critical benchmarks for testing and improving these models. The future holds many more such benchmarks as ongoing orbital monitoring efforts have only begun to yield new dynamical masses from the large samples of ultracool dwarfs discovered by wide field surveys nearly a decade ago.

We gratefully acknowledge the Keck AO team for their exceptional efforts in bringing the AO system to fruition. It is a pleasure to thank Antonin Bouchez, David LeMignant, Marcos van Dam, Al Conrad, Randy Campbell, Carolyn Parker, Joel Aycock, Hien Tran, and the Keck Observatory staff for assistance with the observations. We are very thankful for the contribution of Peter Tuthill in establishing aperture masking at Keck. We are grateful to Brian Cameron for making available his NIRC2 distortion solution, Céline Reylé for customized Besançon Galaxy models, and Adam Burrows and Isabelle Baraffe for providing finely gridded evolutionary models. We have benefited from discussions with Michael Cushing about theoretical models and Thierry Forveille about space motions and orbit fitting using ORBIT. We are indebted to Katelyn Allers for assistance in obtaining IRTF/SpeX data. Our research has employed the 2MASS data products; NASA’s Astrophysical Data System; the SIMBAD database operated at CDS, Strasbourg, France; the SpeX Prism Spectral Libraries, maintained by Adam Burgasser at <http://www.browndwarfs.org/spexprism>; and the M, L, and T dwarf compendium housed at <http://DwarfArchives.org> and maintained by Chris Gelino, Davy Kirkpatrick, and Adam Burgasser (Kirkpatrick 2003; Gelino et al. 2004). TJD and MCL acknowledge support for this work from NSF grant AST-0507833, and MCL acknowledges support from an Alfred P. Sloan Research Fellowship. Finally, the authors wish to recognize and acknowledge the very significant cultural role and reverence that the summit of Mauna Kea has always had within the indigenous Hawaiian community. We are most fortunate to have the opportunity to conduct observations from this mountain.

Facilities: Keck II Telescope (LGS AO, NIRC2), HST (WFPC2), VLT (NACO), Gemini-North Telescope (Hokupa‘a), IRTF (SpeX)

REFERENCES

- Allard, F., Hauschildt, P. H., Alexander, D. R., Tamanai, A., & Schweitzer, A. 2001, *ApJ*, 556, 357
- Barber, R. J., Tennyson, J., Harris, G. J., & Tolchenov, R. N. 2006, *MNRAS*, 368, 1087
- Berger, E., et al. 2009, *ApJ*, 695, 310
- Blackwell, D. E., & Shallis, M. J. 1977, *MNRAS*, 180, 177
- Blake, C. H., Charbonneau, D., White, R. J., Marley, M. S., & Saumon, D. 2007, *ApJ*, 666, 1198
- Bouy, H., Brandner, W., Martín, E. L., Delfosse, X., Allard, F., & Basri, G. 2003, *AJ*, 126, 1526
- Brott, I., & Hauschildt, P. H. 2005, in *ESA Special Publication, Vol. 576, The Three-Dimensional Universe with Gaia*, ed. C. Turon, K. S. O’Flaherty, & M. A. C. Perryman, 565
- Burrows, A., et al. 1997, *ApJ*, 491, 856
- Carpenter, J. M. 2001, *AJ*, 121, 2851
- Chabrier, G., Baraffe, I., Allard, F., & Hauschildt, P. 2000, *ApJ*, 542, 464
- Chabrier, G., Baraffe, I., & Plez, B. 1996, *ApJ*, 459, L91
- Close, L. M., Siegler, N., Potter, D., Brandner, W., & Liebert, J. 2002, *ApJ*, 567, L53
- Costa, E., Méndez, R. A., Jao, W.-C., Henry, T. J., Subasavage, J. P., & Ianna, P. A. 2006, *AJ*, 132, 1234
- Crifo, F., Phan-Bao, N., Delfosse, X., Forveille, T., Guibert, J., Martín, E. L., & Reylé, C. 2005, *A&A*, 441, 653
- Cushing, M. C., et al. 2008, *ApJ*, 678, 1372
- Cushing, M. C., Rayner, J. T., & Vacca, W. D. 2005, *ApJ*, 623, 1115
- Cushing, M. C., Vacca, W. D., & Rayner, J. T. 2004, *PASP*, 116, 362
- Cutri, R. M., et al. 2003, 2MASS All Sky Catalog of point sources. (The IRSA 2MASS All-Sky Point Source Catalog, NASA/IPAC Infrared Science Archive. <http://irsa.ipac.caltech.edu/applications/Gator/>)
- Dahn, C. C., et al. 2002, *AJ*, 124, 1170
- Delfosse, X., Forveille, T., Ségransan, D., Beuzit, J.-L., Udry, S., Perrier, C., & Mayor, M. 2000, *A&A*, 364, 217
- Dupuy, T. J., Liu, M. C., & Ireland, M. J. 2009a, *ApJ*, 692, 729
- , 2009b, *ApJ*, 699, 168
- Faherty, J. K., Burgasser, A. J., Cruz, K. L., Shara, M. M., Walter, F. M., & Gelino, C. R. 2009, *AJ*, 137, 1
- Forveille, T., et al. 1999, *A&A*, 351, 619
- Gautier, III, T. N., et al. 2007, *ApJ*, 667, 527
- Gelino, C. R., Kirkpatrick, J. D., & Burgasser, A. J. 2004, *BAAS*, 205
- Ghez, A. M., et al. 2008, *ApJ*, 689, 1044
- Gizis, J. E., Monet, D. G., Reid, I. N., Kirkpatrick, J. D., Liebert, J., & Williams, R. J. 2000, *AJ*, 120, 1085
- Golimowski, D. A., et al. 2004, *AJ*, 127, 3516
- Guenther, E. W., & Wuchterl, G. 2003, *A&A*, 401, 677

- Henry, T. J., Franz, O. G., Wasserman, L. H., Benedict, G. F., Shelus, P. J., Ianna, P. A., Kirkpatrick, J. D., & McCarthy, Jr., D. W. 1999, *ApJ*, 512, 864
- Henry, T. J., & McCarthy, Jr., D. W. 1993, *AJ*, 106, 773
- Ibukiyama, A., & Arimoto, N. 2002, *A&A*, 394, 927
- Jones, H. R. A., Pavlenko, Y., Viti, S., Barber, R. J., Yakovina, L. A., Pinfield, D., & Tennyson, J. 2005, *MNRAS*, 358, 105
- Jones, H. R. A., et al. 2008, in *Society of Photo-Optical Instrumentation Engineers (SPIE) Conference Series*, Vol. 7014, *Society of Photo-Optical Instrumentation Engineers (SPIE) Conference Series*
- Kirkpatrick, J. D. 2003, in *Proceedings of IAU Symposium 211: Brown Dwarfs*, ed. E. Martin, 189
- Kirkpatrick, J. D., Henry, T. J., & McCarthy, Jr., D. W. 1991, *ApJS*, 77, 417
- Krist, J. 1995, in *Astronomical Society of the Pacific Conference Series*, Vol. 77, *Astronomical Data Analysis Software and Systems IV*, ed. R. A. Shaw, H. E. Payne, & J. J. E. Hayes, 349
- Leggett, S. K., Allard, F., Geballe, T. R., Hauschildt, P. H., & Schweitzer, A. 2001, *ApJ*, 548, 908
- Lenzen, R., et al. 2003, in *Presented at the Society of Photo-Optical Instrumentation Engineers (SPIE) Conference*, Vol. 4841, *Society of Photo-Optical Instrumentation Engineers (SPIE) Conference Series*, ed. M. Iye & A. F. M. Moorwood, 944–952
- Liu, M. C., Dupuy, T. J., & Ireland, M. J. 2008, *ApJ*, 689, 436
- Monet, D. G., Dahn, C. C., Vrba, F. J., Harris, H. C., Pier, J. R., Luginbuhl, C. B., & Ables, H. D. 1992, *AJ*, 103, 638
- Rayner, J. T., Toomey, D. W., Onaka, P. M., Denault, A. J., Stahlberger, W. E., Vacca, W. D., Cushing, M. C., & Wang, S. 2003, *PASP*, 115, 362
- Reid, I. N., Kirkpatrick, J. D., Liebert, J., Gizis, J. E., Dahn, C. C., & Monet, D. G. 2002, *AJ*, 124, 519
- Robin, A. C., Reylé, C., Derrière, S., & Picaud, S. 2003, *A&A*, 409, 523
- Rousset, G., et al. 2003, in *Presented at the Society of Photo-Optical Instrumentation Engineers (SPIE) Conference*, Vol. 4839, *Society of Photo-Optical Instrumentation Engineers (SPIE) Conference Series*, ed. P. L. Wizinowich & D. Bonaccini, 140–149
- Ségransan, D., Delfosse, X., Forveille, T., Beuzit, J.-L., Udry, S., Perrier, C., & Mayor, M. 2000, *A&A*, 364, 665
- Seifahrt, A., Röhl, T., Neuhäuser, R., Reiners, A., Kerber, F., Käuff, H. U., Siebenmorgen, R., & Smette, A. 2008, *A&A*, 484, 429
- Simons, D. A., & Tokunaga, A. 2002, *PASP*, 114, 169
- Tegmark, M., et al. 2004, *Phys. Rev. D*, 69, 103501
- Tokunaga, A. T., Simons, D. A., & Vacca, W. D. 2002, *PASP*, 114, 180
- Vacca, W. D., Cushing, M. C., & Rayner, J. T. 2003, *PASP*, 115, 389
- van Dam, M. A., et al. 2006, *PASP*, 118, 310
- West, A. A., Hawley, S. L., Bochanski, J. J., Covey, K. R., Reid, I. N., Dhital, S., Hilton, E. J., & Masuda, M. 2008, *AJ*, 135, 785
- Wizinowich, P. L., et al. 2006, *PASP*, 118, 297
- Wood, M. A., & Oswalt, T. D. 1998, *ApJ*, 497, 870
- Zapatero Osorio, M. R., Martín, E. L., Béjar, V. J. S., Bouy, H., Deshpande, R., & Wainscoat, R. J. 2007, *ApJ*, 666, 1205